








Geophysical Research Letters

RESEARCH LETTER

10.1029/2020GL090375

Direct Observations of Near-Inertial Wave ζ -Refraction in a Dipole Vortex

Leif N. Thomas¹ , Luc Rainville², Olivier Asselin³ , William R. Young³, James Girton² , Caitlin B. Whalen² , Luca Centurioni⁴, and Verena Hormann⁴ 

¹Department of Earth System Science, Stanford University, Stanford, CA, USA, ²Applied Physics Laboratory, University of Washington, Seattle, WA, USA, ³Scripps Institution of Oceanography, University of California San Diego, La Jolla, CA, USA, ⁴Lagrangian Drifter Laboratory, Scripps Institution of Oceanography, University of California San Diego, La Jolla, CA, USA

Key Points:

- We report the first observations of the reduction in lateral scale of near-inertial waves by vorticity gradients
- As their scale shrinks, waves rapidly radiate downward and into regions with anticyclonic vorticity
- Strain in the background flow field had little direct effect on the evolution of the near-inertial waves

Supporting Information:

- Supporting Information S1

Correspondence to:

L. N. Thomas,
leift@stanford.edu

Citation:

Thomas, L. N., Rainville, L., Asselin, O., Young, W. R., Girton, J., Whalen, C. B., et al. (2020). Direct observations of near-inertial wave ζ -refraction in a dipole vortex. *Geophysical Research Letters*, 47, e2020GL090375. <https://doi.org/10.1029/2020GL090375>

Received 14 AUG 2020

Accepted 26 SEP 2020

Accepted article online 26 OCT 2020

Abstract Generated at large horizontal scales by winds, near-inertial waves (NIWs) are inefficient at radiating energy without a shift to smaller wavelengths. The lateral scales of NIWs can be reduced by gradients in the Coriolis parameter (β -refraction) or in the vertical vorticity (ζ -refraction) or by strain. Here we present ship-based surveys of NIWs in a dipole vortex in the Iceland Basin that show, for the first time, direct evidence of ζ -refraction. Differences in NIW phase across the dipole were observed to grow in time, generating a lateral wavelength that shrank at a rate consistent with ζ -refraction, reaching ~ 40 km in 1.5 days. Two days later, a NIW beam with an ~ 13 km horizontal and ~ 200 m vertical wavelength was detected at depth radiating energy downward and toward the dipole's anticyclone. Strain, while significant in strength in the dipole, had little direct effect on the NIWs.

Plain Language Summary Winds blowing over the ocean generate waves, not just the familiar ones that ride along the surface, but another type which travels down into the deep sea. These so-called internal waves can transmit a large amount of wind energy downward and thus are thought to play an important role in sustaining the deep branch of the ocean circulation. When these internal waves are formed, however, they are ineffective at transporting energy because their wavelengths are large, being set by the wind's $\sim 1,000$ km footprint on the ocean. In order for the waves to efficiently radiate energy downward, their wavelengths must shrink. Theory predicts that the interaction of these waves with ocean vortices can lead to a contraction in wavelength and enhanced energy transport. Here we describe observations made in a pair of counterrotating vortices in the Iceland Basin, which confirm this prediction for the first time in the ocean. Ship-based measurements were used to track the evolution of internal waves generated by the passage of a storm. Within 2 days of their formation, the waves' wavelength shrank to ~ 40 km. Two days later, the waves were observed traveling downward and into the clockwise-swirling vortex, in line with theory.

1. Introduction

Near-inertial waves (NIWs), internal waves with frequencies close to the inertial frequency f , explain a large fraction of the energy in high-frequency motions in the ocean (Alford et al., 2016). Originating primarily as wind-forced near-inertial oscillations (NIOs) in the mixed layer, when NIWs propagate into the ocean interior, they can energize the inertial wave continuum through nonlinear interactions and contribute to sustaining the meridional overturning circulation by driving mixing (Barkan et al., 2017; Polzin & Lvov, 2011; Sugiyama et al., 2009; Whalen et al., 2018; Wunsch & Ferrari, 2004). To efficiently radiate energy into the interior, however, the lateral wavelength of NIOs must shrink from the large scales set by the winds since for internal waves, the speed at which energy propagates vertically varies inversely with the square of the lateral wavelength (Gill, 1982).

The shrinking in NIO scale is thought to arise from gradients in f (i.e., β) or the vertical vorticity of a background flow, $\bar{\zeta}$, which produces the effective inertial frequency, $f_{eff} = f + \bar{\zeta}/2$, of the oscillations (Kunze, 1985; Mooers, 1975). These gradients in f or $\bar{\zeta}$ set up lateral differences in wave phase since NIOs separated a short distance from one another oscillate at slightly different frequencies. As a result, the NIOs develop a horizontal wave number, k_h , whose magnitude increases linearly with time at a rate that

is proportional to the gradient in f_{eff} (D'Asaro et al., 1995; van Meurs, 1998). When the NIO phase differences are caused by the meridional variation in f , we will refer to it as β -refraction (D'Asaro, 1989) and ζ -refraction when gradients in vertical vorticity lead to their generation (Young & Ben-Jelloul, 1997).

β -refraction was clearly demonstrated to be active during the seminal Ocean Storms Experiment (D'Asaro et al., 1995). In that experiment, a combination of drifters and moorings distributed over a few degrees of latitude were used to track phase differences in near-surface inertial currents and the subsequent propagation of near-inertial (NI) energy into the interior after the passage of a storm. By fitting a plane wave to the inertial currents, an estimate of the meridional wave number was made. The resultant wave number was negative and decreased linearly with time at a rate consistent with β -refraction. By 10 days after the storm, a beam of NIW energy was observed at 100 m that was accompanied by a decrease in NI energy in the mixed layer, in line with a flux of energy away from the surface. The observed rate of NI energy decay in the mixed layer was 20–40% faster than that predicted by linear theory, however, indicating that the behavior of the waves was not entirely explained by β -refraction.

ζ -refraction of NIWs by mesoscale eddies can significantly enhance the radiative damping of NIW energy in the mixed layer, and in fact, Balmforth and Young (1999) demonstrated that it can explain the discrepancy in the predicted and observed damping times in the Ocean Storms Experiment. Radiation associated with ζ -refraction is heterogeneous and leads to the preferential propagation of NIW energy into regions of anticyclonic vorticity (Klein et al., 2004; Kunze, 1985; Young & Ben-Jelloul, 1997). Once in anticyclones, NIW energy is rapidly fluxed downward through a process which was first termed the inertial chimney effect by Lee and Niiler (1998) but has recently been renamed the inertial drainpipe effect by Asselin and Young (2020) to evoke the image of downward energy propagation in anticyclones.

In addition to vorticity gradients, strain in the mesoscale eddy field can sharpen the lateral scales of NIWs. Because NIWs have inherently weak group velocities, their propagation speeds are low, and therefore, NIW phase can evolve in a similar way to a passive tracer advected by a background flow such that, in regions of strain, lateral gradients in phase can experience exponential growth (Bühler & McIntyre, 2005). In a companion paper, Asselin et al. (2020) demonstrate that in this weakly dispersive limit and for background flows that are barotropic and for NIWs that initially have large lateral scales, NIW phase is slaved to the vorticity such that under strain, gradients in phase, and vorticity increase in lock step, and the horizontal wave number evolves as

$$\mathbf{k}_h(\mathbf{x}, t) = -\frac{t}{2} \nabla_h \bar{\zeta}(\mathbf{x}, t). \quad (1)$$

However, this is only a transient behavior because as the lateral scales of NIWs shrink, their group velocity increases, dispersion is no longer weak, and the waves propagate out of strain regions. This is the *wave escape* mechanism of Rocha et al. (2018) that limits the growth of the horizontal wave vector by strain.

To our knowledge, ζ -refraction and straining of NIWs by mesoscale eddies and the subsequent propagation of the waves out of the mixed layer have never been observed directly. While the modulation and decoherence of NIOs by vertical vorticity (Elipot et al., 2010; Weller, 1982) and the trapping of NIWs in anticyclones (Joyce et al., 2013; Kunze, 1986; Kunze et al., 1995) have been observed, the progression from NIO generation by winds, shrinking of NIO lateral scale by vorticity gradients and strain, to propagation of NIWs into regions of anticyclonic vorticity had not yet been captured observationally. Here we present measurements made in a mesoscale vortex dipole that document this sequence of events.

2. Field Experiment, Forcing, and Mesoscale Eddy Field

The measurements were made in the Iceland Basin as part of the ongoing Near-Inertial Shear and Kinetic Energy in the North Atlantic experiment (NISKINe), the goal of which is to study the dynamics and energetics of NIWs, with a focus on the higher modes, and their interaction with mesoscale and submesoscale flows. The observations presented here are from two surveys made from the *R/V Neil Armstrong* taken near the axis of a dipole vortex (Figure 1a). The location of the surveys was selected using satellite altimetry to find a site where the gradient in vorticity was large and the strain was confluent, that is, where ζ -refraction and advection of the wave field by the mesoscale were likely to be effective. The observations were timed with the passage of an atmospheric front during Survey 1, which will be referred to as the wind event, with

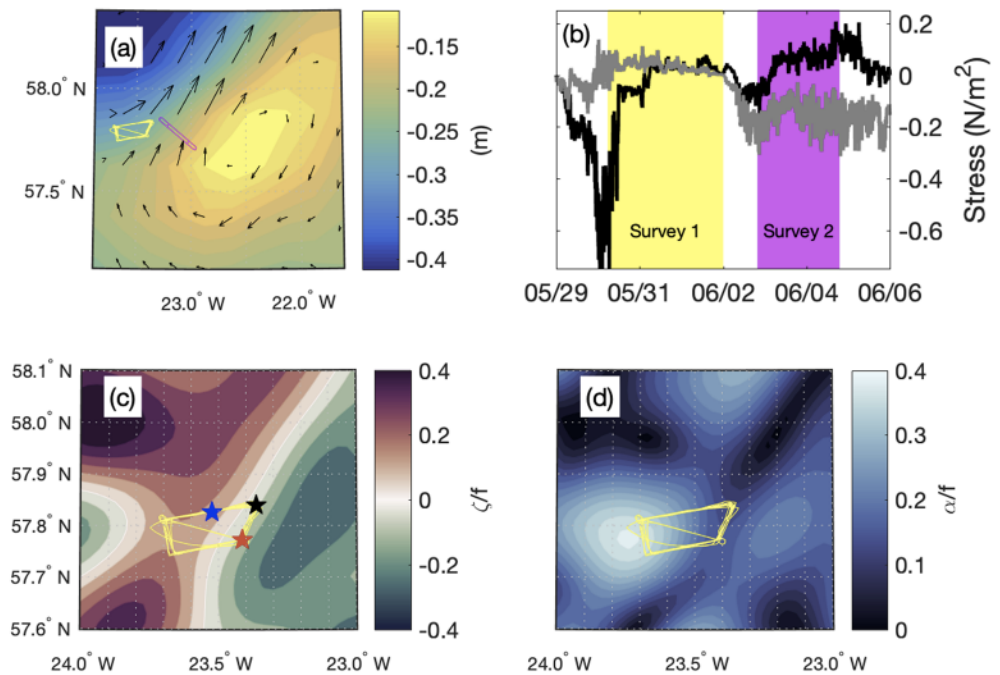


Figure 1. Overview of the eddy field and forcing during the two surveys. (a) Sea surface height (color) and surface geostrophic velocity (vectors) from satellite altimetry and the shiptracks of Survey 1 (yellow) and Survey 2 (magenta). (b) Time series of the zonal (black) and meridional (gray) components of the wind stress during the surveys. (c) The vertical vorticity, ζ , normalized by f , of the horizontally nondivergent component of the near-surface flow (color) and the shiptrack of Survey 1. The red, blue, and black stars are the locations where the time series of velocity shown in Figure 2 were made. (d) The strain rate, α , normalized by f , of the horizontally nondivergent component of the near-surface flow (color) and the shiptrack of Survey 1.

a peak wind stress of 0.7 N m^{-2} at 0:00 on 30 May. Weaker yet more steady winds followed during Survey 2 (Figure 1b).

The observations used in the analysis consist of shipboard velocity measurements and hydrography from CTD casts. Velocity profiles were made with a 150 kHz underway ADCP in the upper 400 m at a resolution of 8 m and a 38 kHz underway ADCP which extended the range of the profiles to over 700 m but at a reduced resolution (24 m). These shipboard velocity measurements were supplemented with currents measured by Lagrangian drifters drogued at 15 m depth (Centurioni, 2018) and were used to construct maps of the horizontally nondivergent component of the velocity field, a proxy for the background flow (\bar{u}, \bar{v}) (see the supporting information for methodology). Within the dipole, the vertical component of the vorticity calculated from the background flow, $\bar{\zeta} = \bar{v}_x - \bar{u}_y$, was characterized by variations of order $0.1f$ distributed over distances of $\sim 10 \text{ km}$, yielding a gradient in vorticity over 100 times greater than β (Figure 1c). The strain rate, $\alpha = \sqrt{(\bar{u}_x - \bar{v}_y)^2 + (\bar{v}_x + \bar{u}_y)^2}$, is similarly of order $0.1f$ (Figure 1d) yielding an e-folding time for the growth of scalar gradients by straining of a few inertial periods.

It is in this background flow that the NIOs generated by the wind event were sampled. During Survey 1, the velocity field was sampled continuously along a looping ship track that straddled the axial jet of the dipole (yellow line in Figure 1c). The sampling was rapid, revisiting the same locations three to four times every inertial period, resulting in unaliased time series of the inertial oscillations. Survey 2 transited from the dipole's axial jet toward its anticyclone (magenta line in Figure 1a), yielding transects of the NIW velocity field and shear. Each transect was completed in less than a quarter of an inertial period and hence was synoptic with respect to the wave's evolution.

3. Evolution of the Horizontal Wave Vector in the Axial Jet

The wind-event produced a clean inertial response that was focused to the upper 50 m. Beneath this depth the flow was nearly barotropic (e.g., Figure S1). To isolate the inertial response, the barotropic flow was subtracted from velocity profiles, and the resultant signal was averaged in the upper 50 m to yield a

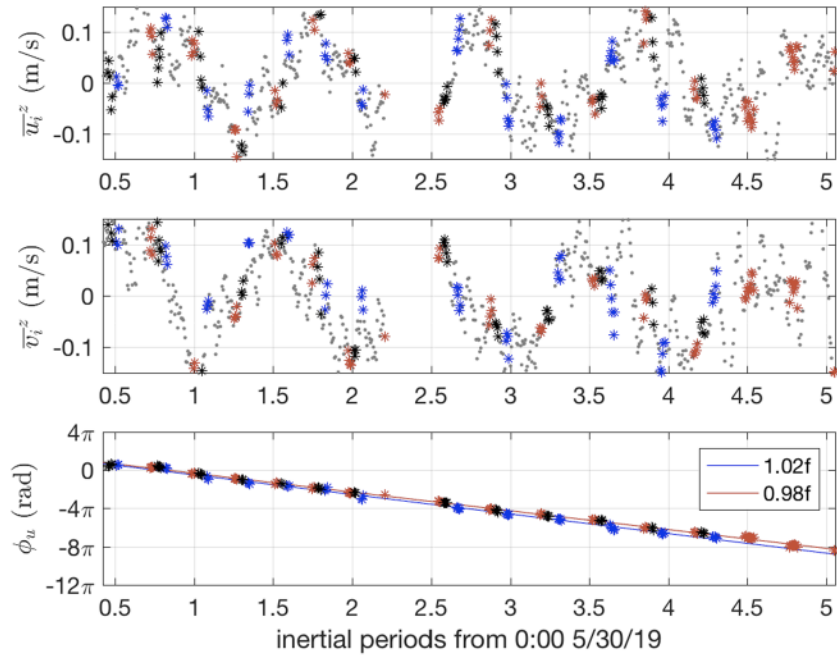


Figure 2. Time series of the zonal, \bar{u}_i^z , (top) and meridional, \bar{v}_i^z , (middle) components of the inertial motions' velocity at three locations in Survey 1 (see Figure 1c), two on the anticyclonic side of the jet (red and black) and the other on the cyclonic side of the jet (blue). The inertial motion velocities from all the locations in Survey 1 are shown in gray. The inertial oscillations on either side of the jet develop phase differences which can be quantified using the angle of the velocity of the inertial motions $\phi_u = \tan^{-1}(\bar{v}_i^z/\bar{u}_i^z)$ (bottom panel), which decreases with time at slightly different rates. Fitting a line to this angle (solid lines) yields a frequency with %95 confidence intervals of $1.02f \pm 0.02f$ and $0.98f \pm 0.01f$ on the cyclonic and anticyclonic side of the jet, respectively.

depth-averaged estimate of the inertial velocity (\bar{u}_i^z, \bar{v}_i^z) (see the supporting information for methodology). Estimates of (\bar{u}_i^z, \bar{v}_i^z) from all locations on Survey 1 trace an inertial oscillation in time, with meridional and zonal velocities of similar magnitude that oscillate in quadrature (Figure 2, gray dots). The signal at three specific locations with differing background vorticity was further analyzed to determine if differences in wave phase could be discerned. Analyses at additional locations on the survey yielded similar results (see Figures S2 and S3). Two of the locations were on the anticyclonic side of the jet separated by a weak gradient in vorticity (red and black stars in Figures 1c and 2), and the third was in a region with cyclonic vorticity (blue stars in Figures 1c and 2). On the cyclonic side of the jet and toward the end of the record, the signal leads the velocity at the other two locations (e.g., \bar{u}_i^z near approximately four inertial periods). At the beginning of the record in contrast, the phase differences between the three time series are not as evident. This can be more carefully quantified by calculating the direction of inertial velocity vector $\phi_u = \tan^{-1}(\bar{v}_i^z/\bar{u}_i^z)$, a measure of wave phase. The angle ϕ_u decreases with time at all three locations, as to be expected for clockwise-rotary inertial motions, but at a faster rate on the cyclonic versus anticyclonic side of the jet (Figure 2, bottom panel). Fitting lines to the time series of ϕ_u yield frequency estimates of $1.02f \pm 0.02f$ and $0.98f \pm 0.01f$ at the locations with cyclonic and anticyclonic vorticity, respectively, in line with the theoretical predictions of Mooers (1975) and Kunze (1985). These slightly different frequencies generate a phase difference between the oscillations on either side of the jet that accumulates over time, leading to the growth of the horizontal wave vector.

The horizontal wave vector was estimated by calculating the phase difference averaged over an inertial period, $\overline{\Delta\phi_u^t}$, divided by the distance, Δs , between the locations:

$$k_{est} = \frac{|\overline{\Delta\phi_u^t}|}{\Delta s}. \quad (2)$$

This estimate was then compared to the theoretical prediction for k_h (1), calculated as

$$k_{th} = \frac{(t - t_0) |\Delta\bar{c}(t)|}{2 \Delta s}, \quad (3)$$

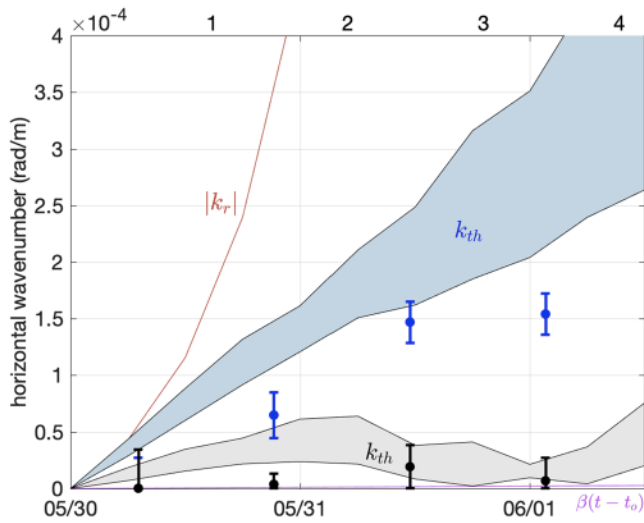


Figure 3. Estimates of the horizontal wave number, k_{est} , (2) calculated from the difference in the phase angle ϕ_u between the locations on Survey 1 indicated by the red and blue stars in Figure 1c separated in the cross-jet direction (blue circles with error bars). Black circles with error bars denote k_{est} calculated between the locations indicated by the red and black stars in Figure 1c, which are separated in the along-jet direction. The theoretical prediction for the evolution of the wave number, k_{th} , (3) calculated using the difference in vorticity between these locations with error estimates is denoted by the shaded blue and gray areas. This is contrasted with a solution to the ray-tracing equations, $|k_r|$, which assumes that the vorticity gradient and strain rate are constant (red line). The wave number that would result if there were no background flow and only β -refraction were active is also shown (magenta line). Time in inertial periods from the peak winds is indicated on the upper x axis of the figure while the date is on the lower x axis.

where $\Delta\bar{\zeta}(t)$ is the time-varying difference in vorticity between the locations and t_0 is the time when the NIO is generated, which is approximated as the time when the winds peaked during the wind event, that is, 0:00 on 30 May. The vorticity difference was calculated using objective maps of the horizontally nondivergent flow field. Uncertainties in mapping parameters and in the velocity data used to create the maps were used to estimate error bounds on k_{th} (see Figure 3 and the supporting information for methodology). Error bars on k_{est} were formed by dividing the standard error of $\Delta\phi_u$ by Δs .

The estimate for the horizontal wave vector in the cross-jet direction increases in time, while there is little obvious growth of the wave vector in the along-jet direction (cf. the blue and black circles in Figure 3). In terms of a horizontal wavelength, $\lambda = 2\pi/k_{est}$, the lateral scale of the waves in the cross-jet direction shrinks to $\lambda \sim 40$ km in 1.5 days. This behavior is qualitatively consistent with the theoretical prediction (3) but is in stark contrast with the strain-driven exponential growth one might expect using a simple solution to the ray-tracing equations for the horizontal component of the wave vector, k_r , that assumes a constant strain rate and vorticity gradient (e.g., red curve in Figure 3 and the supporting information for the details of this solution). Having said this, k_{th} does overestimate the growth of the wave vector in the cross-jet direction. This discrepancy could be due to a breakdown in the assumptions used in the theory, in particular the assumption that the waves are weakly dispersive. Indeed, clear evidence of NIW propagation was observed in Survey 2, suggesting that wave dispersion was not negligible.

4. NIW Propagation Into the Anticyclone

Sections of vertical shear in the zonal and meridional velocities taken early in Survey 2 (specifically, 3.9 days after the wind event) reveal a NIW beam-like structure, with shear bands that tilt downward, suggestive of active wave radiation toward the anticyclonic side of the dipole (Figures 4b and 4d). These sections can be treated as snapshots of the NIW field since they took less than 0.15 inertial periods to complete. As such, the wave vector of the NIWs can be inferred by calculating the spatial gradients of wave phase on the sections. Wave phase was estimated as the angle that the shear vector makes with the horizontal $\phi_{shear} = \tan^{-1}[(\partial v/\partial z)/(\partial u/\partial z)]$. Vertical profiles of ϕ_{shear} indicate that within the beam the shear vector rotates clockwise with depth (e.g., Figure 4c), further evidence of downward energy propagation (Leaman & Sanford, 1975). The profiles suggest that ϕ_{shear} changes by 2π radians over ~ 200 m in the vertical and ~ 2 radians over 4 km at a fixed depth, yielding vertical and horizontal wavelengths of 200 m and 13 km, respectively. These correspond to horizontal and vertical wave numbers $k_h \approx 4.8 \times 10^{-4}$ rad m^{-1} and $m \approx 0.03$ rad m^{-1} , which when substituted into the dispersion relation for NIWs in the presence of vorticity

$$\omega_i = f \left[1 + \frac{1}{2}(Ro + Bu) \right], \quad (4)$$

with $Ro = \bar{\zeta}/f$ and $Bu = N^2 k_h^2 / f^2 m^2$ (Kunze, 1985), and using the section-averaged vorticity $\bar{\zeta} = -0.04f$ and the stratification averaged over the depth range of the beam, $N^2 \approx 4 \times 10^{-6} s^{-1}$ (e.g., Figure 4a), yields an estimate for the intrinsic frequency of $\omega_i \approx 1.01f$. This frequency is larger than $f_{eff} = 0.98f$, indicating that the necessary condition for NIW propagation is met.

Another independent estimate of the intrinsic frequency can be made using the eccentricity of NIW current or shear ellipses. Following the polarization relations for plane NIWs, the intrinsic frequency can be inferred from the ratio of the major to minor axis of the shear ellipse ($u_{z,major}$ and $u_{z,minor}$), namely,

$$\frac{\omega_i}{f} = \frac{u_{z,major}}{u_{z,minor}} \left(1 + \frac{\bar{\zeta}}{f} \right). \quad (5)$$

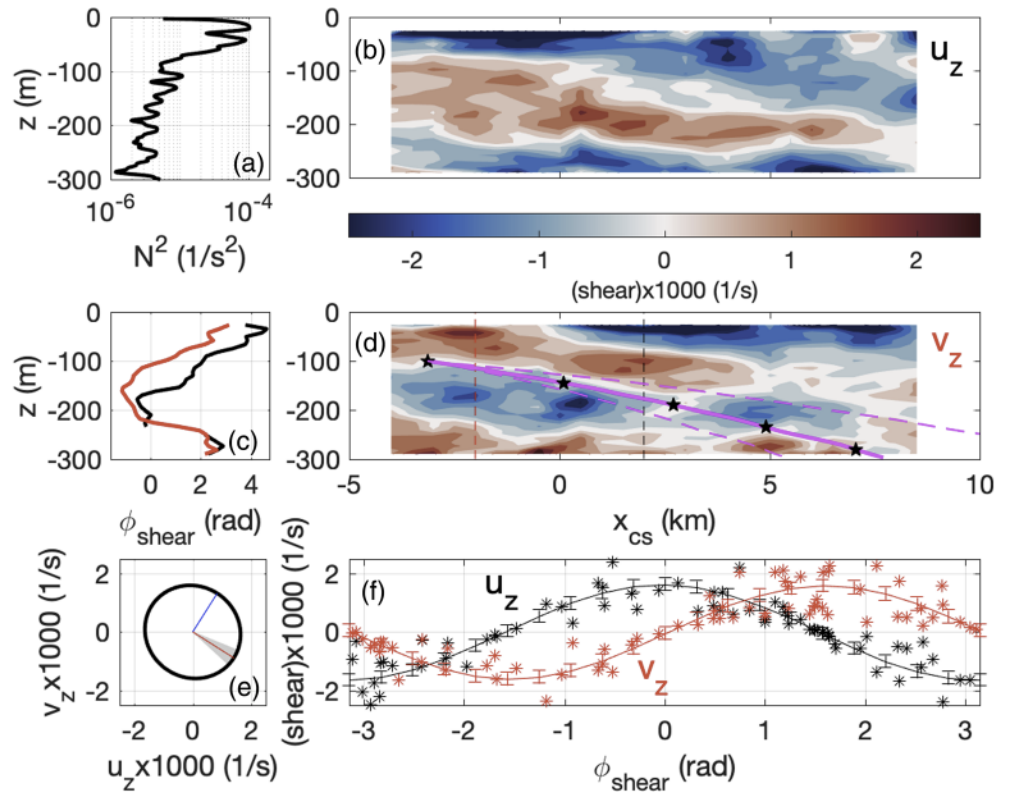


Figure 4. Analysis of a NIW beam propagating down and into the anticyclonic side of the dipole vortex observed on Survey 2. (a) Profile of the square of the buoyancy frequency N^2 . (b) Cross-section sections of the vertical shear in the zonal velocity and (d) meridional velocity, where x_{cs} is the distance in the cross-stream direction (defined to be perpendicular to the speed-weighted average direction of the barotropic flow and where x_{cs} increases moving from the jet toward the anticyclone). Wave rays (solid magenta line) calculated using the mean value of the intrinsic frequency, ω_i , inferred from the eccentricity of the shear ellipse are also plotted in (d). Rays calculated using the upper and lower endpoint values for ω_i at the 95% confidence interval (dashed magenta lines) and the location of a wave packet on the ray each 1 day of travel time (black stars) are also shown. (c) Profiles of the phase angle calculated using the shear, ϕ_{shear} , taken at the locations indicated by the dashed red and black vertical lines in (d). (f) The observed meridional shear (red asterisks) and zonal shear (black asterisks) for all measurements on the section plotted as a function of ϕ_{shear} . Sinusoids fit to the shear are indicated by the solid lines with the 95% confidence interval given by the error bars. (e) Shear ellipse constructed from the sinusoids fit to the observed shear. The major and minor axis of the ellipse are denoted by the red and blue lines, respectively, and the range of ellipse orientation within the 95% confidence interval is indicated by the gray shaded region.

Shear ellipses were calculated by fitting sinusoids to the observed shear as a function of the phase angle ϕ_{shear} using data from all depths and cross-stream positions within the beam (Figure 4f). The fits were then used to construct a shear ellipse, from which the major and minor axis and ellipse orientation, and hence intrinsic frequency and NIW propagation direction, were extracted (Figure 4e). A bootstrap method (see the supporting information for details) was then employed to estimate confidence intervals on these wave properties, yielding mean, upper, and lower endpoint values at the 95% confidence level of $1.026f$, $1.052f$, and $1.000f$, respectively, for the intrinsic frequency and -32° , -20° , -44° for the propagation direction. These intrinsic frequencies are slightly superinertial and imply NIW propagation, consistent with the inference from the dispersion relation. The orientation of the shear ellipse further suggests that the horizontal direction of propagation is to the east-southeast, nominally down the gradient in vorticity of the axial jet of the dipole $-\nabla\zeta$, which averaged over the survey points toward -27° (e.g., Figure 1c).

Apart from direction, the speed of NIW propagation was estimated using ray tracing (see the supporting information for details). Wave rays corresponding to $\omega_i = 1.026f$, $1.052f$, and $1.000f$ approximately align with the slope of the shear bands in the NIW beam (Figure 4d), an additional consistency check on the inferred intrinsic frequencies. For $\omega_i = 1.026f$, ray tracing suggests that wave energy descends ~ 130 m in 4 days, in line with the observed depth of penetration of the NIW beam 3.9 days after the wind event.

5. Discussion

The behavior of the NIW field within the dipole vortex described above is in agreement with the theory and simulations of Asselin et al. (2020). Following their work, the evolution of the NIWs can be conceptualized as a two-step process. The process begins with a nondispersive stage, postinjection of inertial energy by the winds, where wave phase is locked to vorticity and the wave vector grows with the gradient in vorticity. This is followed by a wave escape stage where NIWs radiate downward and away from regions of vorticity gradients and strain. In the nondispersive stage the effects of strain are surprisingly muted. Strain can modify the vorticity gradient and hence ζ -refraction, but it does not lead to exponential growth of the wave vector. This dynamics is played out in the observations. The growth in the wave vector follows the theoretical prediction of Asselin et al. (2020), (1) more closely than the exponential increase in wave vector one would predict from a solution to the ray-tracing equations for a background flow with constant strain rate and vorticity gradient (cf. the blue shaded region with the red curve in Figure 3).

The transition from the nondispersive to the wave escape stage occurs when dispersion becomes stronger than the effects of ζ -refraction and advection. The latter is measured by the Rossby number, Ro , while dispersion scales with the wave Burger number Bu . When the ratio of these two nondimensional numbers $Bu/|Ro|$ is equal to or greater than one, conditions are favorable for wave escape (Asselin et al., 2020; Rocha et al., 2018). These conditions appear to have been met in the observed NIW beam. The inferred intrinsic frequency in the beam is very near f , which from the dispersion relation (4) implies $Ro + Bu \approx 0$, and hence $Bu/|Ro| \approx 1$.

While the intrinsic frequency is near f , it is apparent from the confidence intervals on ω_i that the frequency is biased superinertial. What is the physics that selects this frequency? We hypothesize that the effective inertial frequency at the location where the vorticity gradient is largest sets the intrinsic frequency of the beam since it is there where the horizontal wave number grows the fastest and where wave energy would radiate most rapidly. The observations support this hypothesis. The maximum in $|\nabla_h \bar{\zeta}|$ calculated from the vorticity field averaged over the duration of Survey 1 is located on the cyclonic side of the jet where $f_{eff} = 1.03f$, a value which is close to the mean value of ω_i in the beam.

The other wave property of the beam that merits discussion is the vertical wavelength. The ~ 200 m vertical wavelength in the beam exceeds the vertical extent of the NIOs observed in Survey 1 (e.g., Figure S1), which at first glance might be surprising. However, the surface-intensified nature of these NI motions implies that they project onto a spectrum of waves with different vertical wavelengths. In such a spectrum, for a given horizontal wave number, the waves with larger vertical wavelengths propagate downward more quickly. Hence, at a fixed depth, as wave energy is radiated down from the surface, the waves with longer wavelengths would be expected to be observed first. This qualitative behavior is seen in the simulations of Asselin et al. (2020), but their theory can go further to quantify the evolution of m . For the barotropic flows they considered, the intrinsic frequency of the waves is conserved following a wave group; therefore, as k_h increases via ζ -refraction, so too must the vertical wave number to keep $Ro + Bu$ constant. As a consequence, a spectrum of waves originating from the near surface with different m radiate down in a well-defined sequence of vertical wave numbers that are slaved to $k_h(t)$. While the temporal evolution of m was not inferred from the observations, the fact that the intrinsic frequency of the NIWs stayed close to f in spite of the observed growth in the horizontal wave number is consistent with the theory of Asselin et al. (2020).

6. Conclusions

We have described observations of the evolution of wind-generated NIWs within a dipole vortex in the Iceland Basin where vorticity gradients and, to a lesser degree, strain acted to shrink the waves' lateral scales and drive propagation. The process is analogous to β -refraction which was observed in the Ocean Storms Experiment (D'Asaro et al., 1995) but acts on smaller scales and at a much more rapid pace. For example, ζ -refraction at the axial jet of the dipole vortex resulted in the compression of the NIW lateral scales to 40 km in 1.5 days, compared to ~ 50 km in 20 days in the Ocean Storms Experiment (e.g., the magenta line in Figure 3). In both experiments a downward-propagating beam of NIW energy was observed. In the dipole the beam reached depths greater than 200 m on the anticyclonic side of the axial jet after 4 days, in contrast to ~ 100 m in 20 days for the beam described in D'Asaro et al. (1995). ζ -refraction and advection are clearly more effective at radiating NIW energy away from the surface than β -refraction and can thus play an

important role in the energy budgets of NI motions in the mixed layer given that mesoscale eddies are ubiquitous in the ocean.

Data Availability Statement

The data used in the analyses described in this article can be found online (<https://hdl.handle.net/1773/45636>).

Acknowledgments

We are grateful to the captain and crew of the R/V *Neil Armstrong*, who made the collection of these observations possible. This work was supported by ONR Grants N00014-18-1-2798 (L. N. T.), N00014-18-1-2780 (L. R.), N00014-18-1-2803 (O. A. and W. R. Y.), N00014-18-1-2445 (L. C. and V. H.), and N00014-18-1-2598 (J. B. G. and C. B. W.) under the Near-Inertial Shear and Kinetic Energy in the North Atlantic experiment (NISKINE) Departmental Research Initiative. The drifters used in this study were funded by ONR Grant N00014-17-1-2517 and NOAA Grant NA150AR4320071 “The Global Drifter Program.” We would also like to acknowledge the rest of the scientists involved in NISKINE, especially the leadership team Jennifer MacKinnon, Matthew Alford, Harper Simmons, and Craig Lee, who were instrumental in initiating and organizing the DRI.

References

- Alford, M. H., MacKinnon, J. A., Simmons, H. L., & Nash, J. D. (2016). Near-inertial internal gravity waves in the ocean. *Annual Review of Marine Science*, 8(8), 95–123.
- Asselin, O., Thomas, L. N., Young, W. R., & Rainville, L. (2020). Refraction and straining of near-inertial waves by barotropic eddies. *Journal of Physical Oceanography*, 1–48. <https://doi.org/10.1175/JPO-D-20-0109.1>
- Asselin, O., & Young, W. R. (2020). Penetration of wind-generated near-inertial waves into a turbulent ocean. *Journal of Physical Oceanography*, 50(6), 1699–1716.
- Balmforth, N. J., & Young, W. R. (1999). Radiative damping of near-inertial oscillations in the mixed layer. *Journal of Marine Research*, 57, 561–584.
- Barkan, R., Winters, K. B., & McWilliams, J. C. (2017). Stimulated imbalance and the enhancement of eddy kinetic energy dissipation by internal waves. *Journal of Physical Oceanography*, 47, 181–198.
- Bühler, O., & McIntyre, M. (2005). Wave capture and wave-vortex duality. *Journal of Fluid Mechanics*, 534, 67–95.
- Centurioni, L. R. (2018). Drifter technology and impacts for sea surface temperature, sea-level pressure, and ocean circulation studies. In R. Venkatesan, A. Tandon, E. D’Asaro, M. A. Atmanand (Eds.), *Observing the Oceans in Real Time* (pp. 37–57). Cham, Switzerland: Springer International Publishing.
- D’Asaro, E. A. (1989). The decay of wind-forced mixed layer inertial oscillations due to the β effect. *Journal of Geophysical Research*, 94, 2045–2056.
- D’Asaro, E. A., Eriksen, C. C., Levine, M. D., Niiler, P., Paulson, C. A., & Meurs, P. V. (1995). Upper-ocean inertial currents forced by a strong storm. Part I: Data and comparisons with linear theory. *Journal of Physical Oceanography*, 25, 2909–2936.
- Eliot, S., Lumpkin, R., & Prieto, G. (2010). Modification of inertial oscillations by the mesoscale eddy field. *Journal of Geophysical Research*, 115, C09010. <https://doi.org/10.1029/2009JC005679>
- Gill, A. E. (1982). *Atmosphere-ocean dynamics*. San Diego: Academic Press, Inc.
- Joyce, T., Toole, J., Klein, P., & Thomas, L. (2013). A near-inertial mode observed within a Gulf Stream warm core ring. *Journal of Geophysical Research: Oceans*, 118, 1797–1806. <https://doi.org/10.1002/jgrc.20141>
- Klein, P., Llewellyn-Smith, S., & Lapeyre, G. (2004). Organization of near-inertial energy by an eddy field. *Quarterly Journal of the Royal Meteorological Society*, 130, 1153–1166.
- Kunze, E. (1985). Near-inertial wave propagation in geostrophic shear. *Journal of Physical Oceanography*, 15, 544–565.
- Kunze, E. (1986). The mean and near-inertial velocity fields in a warm-core ring. *Journal of Physical Oceanography*, 16, 1444–1461.
- Kunze, E., Schmidt, R. W., & Toole, J. M. (1995). The energy balance in a warm-core ring’s near-inertial critical layer. *Journal of Physical Oceanography*, 25, 942–957.
- Leaman, K. D., & Sanford, T. B. (1975). Vertical energy propagation of internal waves: A vector spectral analysis of velocity profiles. *Journal of Geophysical Research*, 80, 1975–1978.
- Lee, D. K., & Niiler, P. P. (1998). The inertial chimney: The near-inertial energy drainage from the ocean surface to the deep layer. *Journal of Geophysical Research*, 103, 7579–7591.
- Mooers, C. N. K. (1975). Several effects of a baroclinic current on the cross-stream propagation of inertial-internal waves. *Geophysical Fluid Dynamics*, 6, 245–275.
- Polzin, K. L., & Lvov, Y. V. (2011). Toward regional characterizations of the oceanic internal wavefield. *Reviews of Geophysics*, 49, RG4003. <https://doi.org/10.1029/2010RG000329>
- Rocha, C. B., Wagner, G. L., & Young, W. R. (2018). Stimulated generation: Extraction of energy from balanced flow by near-inertial waves. *Journal of Fluid Mechanics*, 847, 417–451.
- Sugiyama, Y., Niwa, Y., & Hibiya, T. (2009). Numerically reproduced internal wave spectra in the deep ocean. *Geophysical Research Letters*, 36, L07601. <https://doi.org/10.1029/2008GL036825>
- van Meurs, P. (1998). Interactions between near-inertial mixed layer currents and the mesoscale: The importance of spatial variabilities in the vorticity field. *Journal of Physical Oceanography*, 28, 1363–1388.
- Weller, R. A. (1982). The relation of near-inertial motions observed in the mixed layer during the JASIN (1978) experiment to the local wind stress and to the quasi-geostrophic flow field. *Journal of Physical Oceanography*, 12, 1122–1136.
- Whalen, C. B., MacKinnon, J. A., & Talley, L. D. (2018). Large-Scale impacts of the mesoscale environment on mixing from Wind-Driven internal waves. *Nature Geoscience*, 11, 842–847.
- Wunsch, C., & Ferrari, R. (2004). Vertical mixing, energy, and the general circulation of the oceans. *Annual Review of Fluid Mechanics*, 36, 281–314.
- Young, W. R., & Ben-Jelloul, M. (1997). Propagation of near-inertial oscillations through a geostrophic flow. *Journal of Marine Research*, 55, 735–766.